Coherent storage and manipulation of broadband photons via dynamically controlled Autler–Townes splitting

Erhan Saglamyurek[1]*, Taras Hrushevskyi[1], Anindya Rastogi[1], Khabat Heshami [2] and Lindsay J. LeBlanc [1,3]*

Photonic quantum information technologies rely on quantum memory for long-lived storage and coherent manipulation of short pulses of non-classical light. The optical quantum memories explored over the past two decades are based on various coherent light–matter interaction schemes, but despite impressive progress, practical memories featuring efficient, broadband and long-lived operation remain elusive, due to the technical demands and inherent limitations of the established schemes. Here, we introduce a technique for high-speed quantum memory and manipulation that overcomes these obstacles. This scheme relies on dynamically controlled absorption of light via the 'Autler–Townes effect', which mediates reversible transfer between photonic coherence and the collective ground-state coherence of the storage medium. We experimentally demonstrate proof-of-concept storage and signal processing capabilities of our protocol in a laser-cooled gas of rubidium atoms, including storage of nanoseconds-long single-photon-level laser pulses for up to a microsecond. This approach opens up new avenues in quantum optics, with immediate applications on atomic and solid-state platforms.

When a strong electromagnetic field resonantly drives a transition, that transition can be split into a doublet due to the dynamic, or a.c., Stark effect of the field, as first reported by Autler and Townes[1]. This effect can be directly probed using a weak electromagnetic field that couples the split levels to a third level (Fig. 1a–c). Since its discovery, this splitting, commonly referred to as Autler–Townes splitting (ATS), has been observed in numerous atomic and molecular media[2,3], and extensively studied to describe underlying quantum optical phenomena in laser cooling, cavity quantum electrodynamics[4–6] and high-resolution spectroscopy[7–9].

In the context of coherent storage and manipulation of light with matter, remarkable advances have been made possible by electromagnetically induced transparency (EIT), which relies on quantum interference[10,11]. The ATS regime emerges when this quantum interference is washed out due to the strong electromagnetic fields, leading to broadening of the narrow spectral transparency window associated with EIT. The nature of the crossover between EIT and ATS is an active topic of research[12–18], begging the question of whether it is possible to directly leverage ATS for coherent control of light beyond treatment as an unfavourable EIT regime. Apart from a theoretical proposal for a photon-echo interaction in the ATS regime[19], this possibility remains unexplored.

Here, we develop an approach where absorption of light pulses by dynamically controlled ATS lines mediates coherent storage, which is intrinsically suitable for efficient, broadband and long-lived quantum memories. We demonstrate an experimental implementation of our protocol in a Λ-type three-level system of cold Rb atoms by reversibly mapping coherence from nanoseconds-long weak laser pulses onto collective spin states of atoms for up to a microsecond of storage. We show that, compared with established techniques[20–26], our scheme is situated in a favourable regime for practical broadband

memories, offering significantly relaxed requirements in terms of optical density, power of the coupling electromagnetic field, technical complexity, and robustness to decoherence and experimental instabilities. Furthermore, we extend this approach to coherent manipulation of optical pulses, demonstrating spectral-temporal pulse shaping, temporal beam-splitting and interferometry. As our approach relies on a generic ATS (without additional control mechanisms or fragile quantum effects as required in EIT), it is readily achievable on diverse platforms, including atomic and molecular vapours[11], Rydberg atoms[27,28], colour centres[29,30], optomechanical systems[31–34] and superconducting quantum circuits[35–38]. These general principles can be further exploited for high-precision spectroscopy, metrology and quantum technologies, including quantum communication and optical quantum computing.

Results

The ATS quantum memory protocol. We begin with a simplified description of our approach for broadband light storage, with further details in Methods. We consider a three-level system in a Λ-configuration involving two long-lived spin levels $|g\rangle$ and $|s\rangle$ in the ground state and an excited state $|e\rangle$ that can be optically coupled to both ground levels, as shown in Fig. 1a (in principle, it is possible to implement this protocol in any three-level configuration with modifications). Assuming that atoms initially populate $|g\rangle$, a weak resonant signal field with Rabi frequency Ω_s couples $|g\rangle$ to $|e\rangle$, and a strong resonant control field drives the transition between $|s\rangle$ and $|e\rangle$ with Rabi frequency Ω_c. The coherence decay rate for the optical transition $|e\rangle \leftrightarrow |g\rangle$ is $\gamma_e = \Gamma/2$, where Γ is the radiative decay rate of state $|e\rangle$, and the rate for the spin transition $|g\rangle \leftrightarrow |s\rangle$ is γ_s. Provided that $\gamma_s \ll \gamma_e$, and that the control field has a Rabi frequency that is ideally much larger than the coherence decay rate of the optical transition ($\Omega_c \gg \gamma_e$), the $|g\rangle \leftrightarrow |e\rangle$ transition exhibits an

[1]Department of Physics, University of Alberta Edmonton, Alberta, Canada. [2]National Research Council Canada, Ottawa, Ontario, Canada. [3]Canadian Institute for Advanced Research, Toronto, Ontario, Canada. *e-mail: saglamyu@ualberta.ca; lindsay.leblanc@ualberta.ca
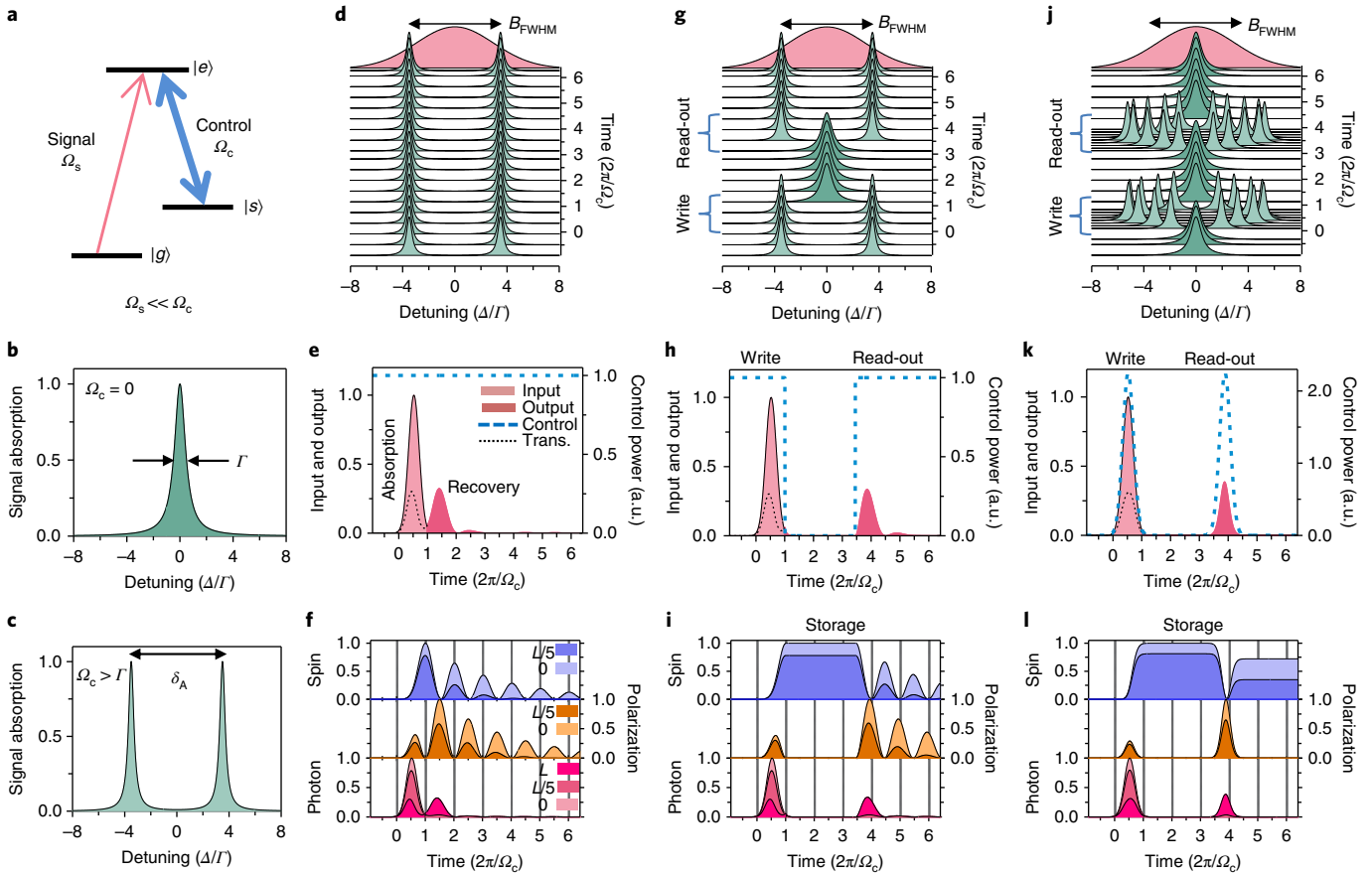
Fig. 1 | ATS quantum memory protocol. a, In a Λ-type three-level system, a strong coupling field (control, blue) and and weak probe field (signal, red) with Rabi frequencies Ω_c and Ω_s drive the transitions $|s\rangle \leftrightarrow |e\rangle$ and $|g\rangle \leftrightarrow |e\rangle$, respectively. **b,** When $\Omega_c = 0$, the absorption on $|g\rangle \leftrightarrow |e\rangle$ is naturally broadened with a linewidth of Γ. **c,** When $\Omega_c > \Gamma$, the natural absorption line is split into two with the peak spacing of $\delta_A \approx \Omega_c$ and linewidths $\Gamma/2$ via the Autler–Townes effect. Here, $\Omega_c = 7\Gamma$. **d–l,** Descriptions of three configurations for the ATS memory scheme, presented with spectral dynamics in **d, g** and **j,** temporal evolution of the input/output signals and control fields in **e, h** and **k,** and coherence dynamics in **f, i** and **l.** For the constant control configuration (**d–f**), a control field (blue dashed line in **e**), on at all times, generates a static ATS. An input signal pulse with bandwidth $B_{FWHM} = \Omega_c/2\pi$ (pink curve in **d**) is partially absorbed with a transmitted portion (black dotted curve in **e**) and repetitively recovered as output signals with delays of $2\pi/\Omega_c$ as shown here for $\Omega_c = 7\Gamma$, $d = 13$ and $\gamma_s = 0$. Oscillatory system dynamics of coherence in spin ($|S(z,t)|^2$), polarization ($|P(z,t)|^2$) and photonic ($|E(z,t)|^2$) components, near the entrance (light) and exit (dark) of the atomic medium are shown in **f.** Storage and on-demand recall of the signal with an interrupted control configuration are illustrated in **g–i.** The control is switched off just before the first recovery (write), and switched back on at $T = 3.5(2\pi/\Omega_c)$ (read-out). Write and read-out via pulsed control fields are presented in **j–l.** Here, we illustrate this using control fields with the same Gaussian profile as the signal, and with peak $\Omega_c^{peak} = 10.5\Gamma$ to ensure the area $A_c(\tau) = 2\pi$.

ATS whose peaks are separated by $\delta_A \approx \Omega_c$ (see Fig. 1b,c). Note that the amount of ATS can be dynamically changed using the control field power such that $\Omega_c(t) \approx \delta_A(t) = \alpha\sqrt{\mathcal{P}(t)}$, where α is a system-specific proportionality constant and $\mathcal{P}(t)$ is the control power. This feature plays an important role in the operation of our memory scheme, as detailed later.

For the ATS regime described above, we analyse the dynamics of the resonant atom–light system for N uniformly distributed atoms using the Maxwell–Bloch equations[19,39,40]:

$$(\partial_t + c\partial_z)\hat{E}(z,t) = ig\sqrt{N}\hat{P}(z,t) \qquad (1)$$

$$\partial_t\hat{P}(z,t) = -\gamma_e\hat{P}(z,t) + ig\sqrt{N}\hat{E}(z,t) + \frac{i}{2}\Omega_c\hat{S}(z,t) \qquad (2)$$

$$\partial_t\hat{S}(z,t) = -\gamma_s\hat{S}(z,t) + \frac{i}{2}\Omega_c^*\hat{P}(z,t) \qquad (3)$$

where $\hat{E}(z,t)$ is the time- (denoted by t) and position- (denoted by z) dependent electric field operator for the photonic field, and $\hat{P}(z,t)$ and $\hat{S}(z,t)$ are the time- and position-dependent polarization and spin-wave operators, which are described by the collective atomic coherences of $|g\rangle \leftrightarrow |e\rangle$ and $|g\rangle \leftrightarrow |s\rangle$, respectively[40]. The strength of the atom–light coupling is $g\sqrt{N} = \sqrt{cd\gamma_e/2L}$, where g is the coupling constant, d is the peak optical depth, c is the the speed of light in vacuum, and L is the length of the atomic medium along z, which is the propagation direction of the photonic field. In the context of photon storage and recall, equations (1)–(3) can be used to describe mapping coherence from an input (signal) photonic mode $\hat{E}^{in}(z,t) = \hat{E}(0,t)$ (with a slowly varying temporal envelope over period $[0, \tau]$ such that $\partial_t\hat{E}(z,t) \approx 0$) to a spin-wave mode $\hat{S}(z,t > \tau)$, and after a storage time T, back to an output photonic mode $\hat{E}^{out}(z,t) = \hat{E}(L, t > T)$. This reversible transfer between the photonic and spin components of the system is mediated by the evolution of the polarization $\hat{P}(z,t)$ and controlled by $\Omega_c(z,t)$ (with a complex conjugate, denoted by $\Omega_c^*(z,t)$), which together with

$g\sqrt{N}$, γ_e and γ_s, determine the output photonic mode. We note that the results of this treatment are applicable to both weak classical photonic fields (provided that $\Omega_s \ll \Omega_c$ and the photon number is much smaller than N) and quantum fields, including single-photon excitations; as such we represent from here forth those operators as fields: $\hat{E} \to E$.

With the goal of highly efficient broadband light storage and retrieval under favourable conditions (that is, moderate optical depths and control intensities), we investigate three related configurations for the timing of the input signal and control fields (Fig. 1e–k), each associated with the spectral domain (Fig. 1d–j) and dynamical (Fig. 1f–i) descriptions of the atom–light system. In the first configuration (Fig. 1d–f), a control field with constant power (constant Ω_c) generates a fixed ATS for all times. At $t = 0$, a short Gaussian signal pulse whose bandwidth spans the ATS enters the medium (defining the input photonic mode $E(0,t)$). In our protocol, we specify the following relationship between the signal bandwidth and ATS (Fig. 1d): $\delta_A/2\pi = \Omega_c/2\pi = B_{FWHM}$, where B_{FWHM} is the characteristic signal bandwidth at full-width half-maximum (FWHM), and $\tau_{FWHM} = 0.44/B_{FWHM}$ is the corresponding time of the signal. As the signal propagates through the medium, it is partially or fully absorbed by the ATS peaks, and the coherence carried by the signal pulse is mapped onto the spin excitations over the total duration of the pulse $\tau \approx 2.25\tau_{FWHM}$. Immediately after this mapping is complete, the signal pulse is coherently recovered between $t = \tau$ and $t = 2\tau$, as shown in Fig. 1e. An essential feature in this protocol arises from the spectral matching between ATS and the signal bandwidth ($2\pi B_{FWHM}/\Omega_c = 1$): the pulse area for the control field $A_c(t) \cong \int_0^t \Omega_c(t')dt'$ during the absorption and recovery, both with time τ, is

$$A_c(\tau) = \Omega_c(2.25\tau_{FWHM}) = \Omega_c\left[2.25\left(\frac{0.44}{B_{FWHM}}\right)\right] \approx 2\pi \qquad (4)$$

Complete analysis of the atom–light system dynamics (illustrated in Fig. 1f) show that the storage (absorption) and recovery processes rely on the time-dependent oscillatory exchange of the coherence between the spin and photonic components mediated by the polarization component with a period $2\pi/\Omega_c$, as described by the equations[19]

$$|S(z,t)|^2 \propto \cos^2[A_c(t)/2] \qquad (5)$$

$$|E(z,t)|^2 \propto \sin^2[A_c(t)/2] \qquad (6)$$

$$|P(z,t)|^2 \propto \sin^2[A_c(t)/2] \qquad (7)$$

As the coherence, initially carried by the input signal mode, reversibly evolves between the spin-wave and photonic modes inside the medium, it is mapped onto a delayed output signal mode (at $z = L$) for those times when the control pulse area $A_c(t) = 2\pi n$ (where $n = 1, 2, 3…$). Specifically, the initial coherence is transferred to the spin-wave mode in the first cycle ($n = 1$, absorption), and it is converted back to a (output) photonic mode in the second cycle ($n = 2$, recovery) after a delay $T_{delay} = 2\pi/\Omega_c \approx \tau$. In general, some coherence remains as a spin-wave after the first recovery, and is periodically retrieved (with smaller amplitude) as additional output signals at intervals of T_{delay}.

In the second timing configuration, we convert this pre-determined delay (T_{delay}) into an on-demand signal retrieval process with adjustable storage time, T. As illustrated in Fig. 1g–i, this can be achieved by switching off the control field just before the recovery starts, and switching it back on after a desired time, which are

referred to as 'write' and 'read-out' processes, respectively. The writing process transfers the optical coherence to the spin-wave mode (in the first 2π control pulse area, $A_c^{write}(\tau)$) and traps it in the medium by decoupling the control. Then, after a storage time T, a second 2π control pulse area ($A_c^{read}(\tau)$) initiates the reading process and the stored coherence is released as the output photonic mode.

In the third timing configuration, we store and retrieve signal pulses with time-varying power (equivalently, $\Omega_c(t)$) of the write and read-out fields, for pulsed operation of the ATS memory (Fig. 1j–l). Since the dynamics depend only on $A_c(\tau)$ (equations (5)–(7)) and not the specific time-dependence of $\Omega_c(t)$, the coherence transfers from the photonic to spin mode, and back, each time $A_c^{write}(\tau) = A_c^{read}(\tau) = 2\pi$. For example, writing and read-out can be accomplished by using control pulses with the same temporal profile as the input signal, as shown in Fig. 1k. This pulsed operation of ATS memory can be exploited for quantum signal processing, including temporal beam-splitting and pulse shaping, which have been already demonstrated with other memory schemes[41], though with high demand and technical complexity, as detailed in the next sections.

The efficiency for storage followed by recall (memory efficiency, η) can approach unity under appropriate conditions, as detailed in Methods. First, optical depth must be sufficiently large. Second, the control Rabi frequency Ω_c must be large and spatially uniform, satisfying $F = \Omega_c/\Gamma \gg 1$ (where we define F as the 'ATS factor'), while maintaining the pulse areas $A_c^{write}(\tau) = A_c^{read}(\tau) = 2\pi$. Note that because the memory's acceptance bandwidth is directly determined by Ω_c ($B_{FWHM} \approx \Omega_c/2\pi$, which can be chosen at will), the requirement of large F makes the ATS memory protocol intrinsically suitable for efficient and broadband operation. However, as shown in Fig. 2a, the maximum efficiency for the first-order recall ($n = 2$) is limited to 54% due to the re-absorption of retrieved light inside the medium, as in other resonant absorption-based memory protocols such as photon-echo-based techniques[42,43]. Therefore, the third condition for large efficiency is to eliminate re-absorption, which is possible, for example, by using backward retrieval via counter-propagating write and read-out control fields[40,42]. In this arrangement, as shown in Fig. 2b, near-unity memory efficiency ($\eta \approx 0.9$) is possible for broadband signal pulses ($B_{FWHM} \geq 10\Gamma/2\pi$) at moderate optical depths ($d \geq 85$), which is technically feasible in several platforms[44–46]. Compared with established techniques, the inherently fast and all-optically controlled operation of ATS memory provides optimal conditions for broadband light storage with significantly relaxed technical requirements.

Experimental setup and ATS characterization. We demonstrate a proof-of principle of the ATS memory protocol using an ensemble of ~2.5×10^8 cold ^{87}Rb atoms released from a magneto-optical trap (MOT). Figure 3a,b shows a simplified diagram of our experimental setup, detailed in Supplementary Sections 1–3. In this system, we construct a Λ-configuration using two ground hyperfine levels ($F = 1, 2$ as $|g\rangle$ and $|s\rangle$ with spacing of 6.83 GHz) and one excited ($F' = 2$ as $|e\rangle$) level of the D2 transition (780 nm). Nearly co-propagating signal and control fields (derived from different continuous-wave lasers whose amplitudes, frequencies and phases are controlled via acousto-optic modulators) are coupled to the $|F = 1\rangle \to |F' = 2\rangle$ and $|F = 2\rangle \to |F' = 2\rangle$ transitions, respectively. Absorption measurements of the $|F = 1\rangle \to |F' = 2\rangle$ transition without any control field yield a single absorption feature with a peak optical depth of $d^{exp} = 3.0$ to 3.5 and linewidth of $\Gamma^{exp}/2\pi = (7.7 \pm 0.2)$ MHz, including a residual Doppler broadening (upper panel in Fig. 3c). By measuring the same transition in the presence of a strong control field, we observe two well-separated absorption peaks: the manifestation of ATS. Our typical control power $\mathcal{P} = 3.0$ mW gives a peak separation $\delta_A/2\pi = (10.7 \pm 0.3)$ MHz (lower panel in Fig. 3c), showing that our system is predominantly in the ATS regime: $\Omega_c > \Gamma^{exp}$ (refs [13,14]). Note
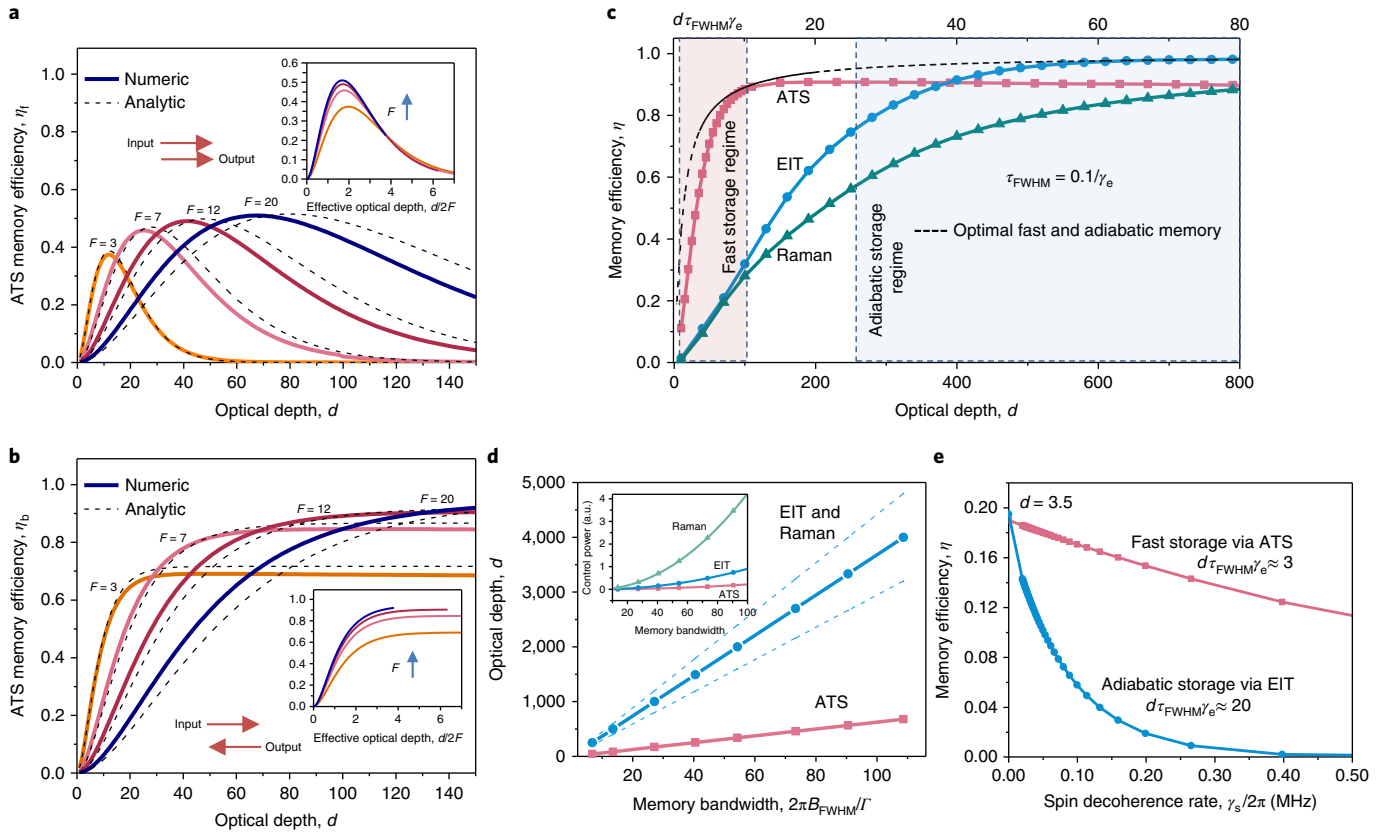
Fig. 2 | Theoretical analysis of ATS memory performance versus established memory protocols. a,b, Numerically calculated ATS memory efficiency versus optical depth for forward-propagating (**a**) and backward-propagating (**b**) output modes, for different $F = \Omega_c/\Gamma$ (solid curves). Analytic calculations of ATS memory efficiency using expressions $\eta_f = (d/2F)^2 e^{-d/2F} e^{-1/F}$ (**a**) and $\eta_b = (1 - e^{-d/2F})^2 e^{-1/F}$ (**b**) are shown with dashed curves for comparison. Inset plots show the same numerical calculations versus effective optical depth, $\tilde{d} = d/2F$. **c,** Numerically calculated memory efficiency versus optical depth for storage of a short Gaussian pulse $\tau_{FWHM} = 0.1/\gamma_e$ ($B_{FWHM} = 13.5\Gamma/2\pi$) via ATS protocol, compared with EIT and off-resonant Raman protocols with optimized parameters in the backward recall scheme. The near-optimal efficiency is obtained at $d\tau_{FWHM}\gamma_e \approx 8$–10 (or $d \approx 80$–100) and $d\tau_{FWHM}\gamma_e \approx 40$–60 (or $d \approx 400$–600) for ATS and EIT/Raman protocols by satisfying the fast and adiabatic operation conditions, respectively. Dashed curve shows maximally achievable memory efficiency for a given optical depth using ATS protocol with optimally short signal pulses ($\tau_{FWHM} = 10/d\gamma_e$) and using EIT protocol with an optimally long signal pulse ($\tau_{FWHM} \approx 20/\gamma_e$), which is in agreement with the universal bounds[39]. **d,** Optical depth versus memory bandwidth ($B_{FWHM} \gg \Gamma/2\pi$) is calculated for near-optimal memory efficiency ($\eta \gtrsim 0.85$) by maintaining $d\tau_{FWHM}\gamma_e = 8$ for ATS (red solid line) and $d\tau_{FWHM}\gamma_e = 50 \pm 10$ for EIT/Raman (blue solid line and dashed bound lines) at each bandwidth. The inset shows the normalized control power requirement of each protocol for each bandwidth. **e,** Memory efficiency versus spin decoherence rate for optimal EIT storage with $\tau_{FWHM} = 300$ ns (blue) and for optimal ATS storage with signal $\tau_{FWHM} = 40$ ns (red) for the shortest possible storage time $T \approx 2.5\tau_{FWHM}$ under the conditions $d = 3.5$ and $\gamma_e/2\pi = 3$ MHz.

that the ATS memory protocol still works in the regimes of $\Omega_c \approx \Gamma$ (the ATS–EIT crossover regime) and $\Omega_c < \Gamma$ (the EIT regime), but with lower efficiencies as discussed in Methods. Further, we characterize the peak separation δ_A with respect to the control power as shown in Fig. 3d.

Demonstration of ATS memory in cold atoms. We implement the ATS memory using the three timing configurations described above. First, we examine the absorption and recovery of a short Gaussian signal pulse with a peak power of $\approx 30\,\mu W$ in the presence of constant control power ($\mathcal{P} = 3.0\,mW$), which generates a static ATS, as shown in Fig. 3c. The signal bandwidth $B_{FWHM} = 11\,MHz$ ($\tau_{FWHM} = 40\,ns$) fulfills the bandwidth-matching condition: $B_{FWHM} \approx \delta_A/2\pi = \Omega_c/2\pi$ (red dashed trace in Fig. 3c). We observe that on entering the medium, the pulse is partially absorbed and then is emitted with $\eta^{exp} = 13.0\%$ after a delay of one pulse duration (Fig. 3e), in good agreement with our simulations based on the numerical analysis with the Maxwell–Bloch equations (see Supplementary Section 6 for details).

To demonstrate the second timing configuration with recall on-demand, we repeat the above procedure but switch off the control

field just before the recovery starts, trapping the coherence in the spin-wave mode. After a storage time $T = 230\,ns$, we switch the control field back on, resulting in on-demand retrieval with $\eta^{exp} = 7.3\%$, as shown in Fig. 3f.

To demonstrate the third timing configuration, corresponding to pulsed operation, a write control field with the same temporal profile and duration as the input signal ($\tau_{FWHM} = 40\,ns$) is temporally overlapped with the input signal inside the medium, which leads to storage. After $T = 230\,ns$, we recall this signal by sending a read-out control pulse with the same Gaussian shape and duration as the write pulse, as shown in Fig. 3g. To maintain the $A_c^{write} = A_c^{read} = 2\pi$ pulse area, we set the peak power to $\mathcal{P}_{peak} = 8.5\,mW$ (corresponding $\Omega_c/2\pi = 17\,MHz$) for the read and write pulses. This gives $\eta^{exp} = 7.8\%$, nearly the same efficiency as obtained in the second configuration.

The main limiting factors to our memory efficiency are large spin-wave decoherence rates ($\gamma_s^{exp}/2\pi = 0.24$ to 0.40 MHz) and small optical depths in our current system. These factors also limit the observed storage times to a microsecond (Supplementary Sections 4 and 5 and Supplementary Fig. 2). However, significant improvement to our memory performance in terms of efficiency,
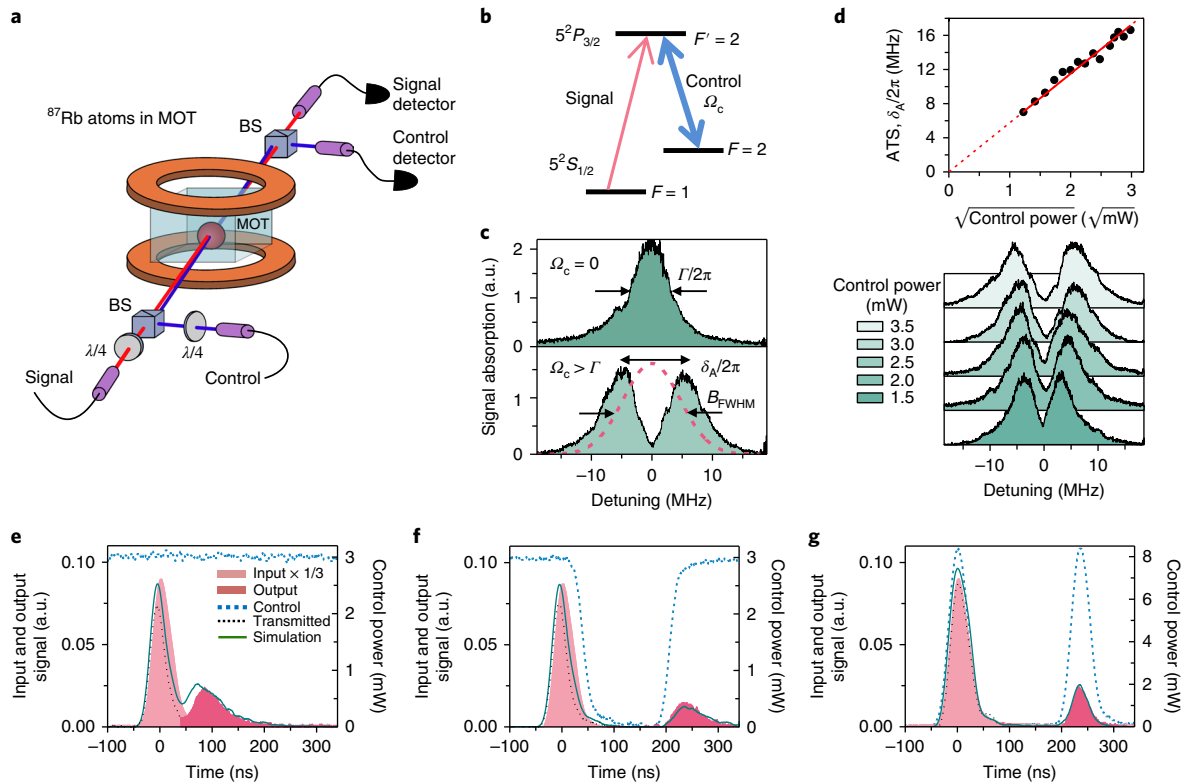
Fig. 3 | Experimental demonstration of ATS memory in cold atoms. a,b, A three-level Λ-system is formed using the D2 transition of ^{87}Rb atoms (**b**) that are cooled down in a MOT (**a**), as detailed in Supplementary Section 1. For storing light or probing ATS features in cold atoms, the linearly polarized signal (red) and control (blue) beams from separate fibre-optics are combined on a free-space beam-splitter (BS), following quarter-waveplates (λ/4) for polarization control. Next, the signal and control beams, with separation angle 2°, overlap inside the atomic cloud. After interaction with the atoms, the signal is coupled to a single-mode fibre for spatial filtering from the control field and directed to a photodiode for detection. A small fraction of the control beam reflected from the output beam-splitter is also detected for pulse synchronization and power calibration. **c,** The transition linewidth (Γ) and a typical ATS ($δ_A$) for $F=1 \leftrightarrow F'=2$ are measured via the absorption of a weak frequency-swept signal, yielding $Γ^{exp}/2π=(7.7\pm0.2)$ MHz for $\mathcal{P}=0$ mW (upper panel) and $δ_A/2π \approx Ω_c/2π=(10.7\pm0.3)$ MHz for $\mathcal{P}=3.0$ mW (lower panel). **d,** The ATS is characterized with respect to control power, showing a good agreement with the linear relation $δ_A/2π = α\sqrt{\mathcal{P}}$, where α is 5.75 MHz/$\sqrt{mW}$. **e–g,** The storage and retrieval of an input signal pulse (bright shaded) with bandwidth $B_{FWHM}=11$ MHz ($τ_{FWHM}=40$ ns), shown with the red dashed line in **c** is demonstrated for the three timing configurations involving constant (**e**), interrupted (**f**) and pulsed (**g**) control fields (blue dashed), which are theoretically described in Fig. 1e, h and k, respectively. The measurement results, including transmitted (black dotted) and recalled signal (dark shaded) are in agreement with the simulations of the Maxwell–Bloch equations (solid green) for experimental input and control traces, and $d^{exp}=3.5$, $Γ^{exp}/2π=7.7$ MHz, $γ_s^{exp}/2π=0.25$ MHz parameters, which were extracted from independent measurements.

storage time and and bandwidth is readily achievable, as detailed in Supplementary Section 5.

Preservation of coherence after storage and recall. Next, we experimentally verify the phase-preserving nature of the ATS memory. To do so, we store and recall $τ_{FWHM}=40$ ns signal pulses prepared with different phase settings ($θ_s$). After each signal pulse, we send a reference pulse at the recall time with the same duration and an unchanged phase setting ($θ_r$). The transmitted part of the reference pulse thus temporally overlaps and interferes with the stored-and-recalled signal pulse (Fig. 4a). As the relative phase between the signal and the reference pulses ($\Delta θ = θ_s - θ_r$) is varied, we observe near perfect constructive and destructive interference with an average visibility of 94% (Fig. 4b), confirming the coherent nature of our memory.

Storage of pulses at the single-photon level. In addition to phase preservation, storage and recall at the single-photon level with low noise is another essential requirement for applications of quantum information. To demonstrate this feature with the ATS memory, we attenuate our 40-ns-long signal pulses before the memory input such that the

average number of photons is reduced from $\bar{n}_{in} \approx 0.5 \times 10^7$ to 0.3 per pulse. To improve spatial filtering of the strong control beam from the single-photon-level signal beam, we increase the angle between them from 2° to 75°, leading to 140 dB isolation. In our demonstrations, we implement pulsed memory operation to store and recall the signal ($\bar{n}_{in}=0.3$) after 200 ns. We measure photon detection counts on our single-photon detector for transmitted and recalled signal pulses in time-resolved fashion using a time-to-digital converter. This measurement is repeated 1,000 times with 1 µs time separation between each storage/recall event for each cold-atom preparation. Figure 4c shows a detection histogram obtained after 500 cycles of cold-atom preparation/measurements. We determine the ratio of the stored-and-recalled signal to noise (SNR) to be 40 ± 10 with a negligibly small noise floor, coming from the stray control field, as shown in the inset. Using this result one can estimate average quantum memory fidelity to be as high as $\mathcal{F}=1-1/SNR=0.97\pm0.01$, if quantum states were stored. Our results hold great promise for interfacing broadband ATS memory with true single-photon sources.

Dynamically controllable storage bandwidth. The acceptance bandwidth of an ATS memory can be dynamically controlled.
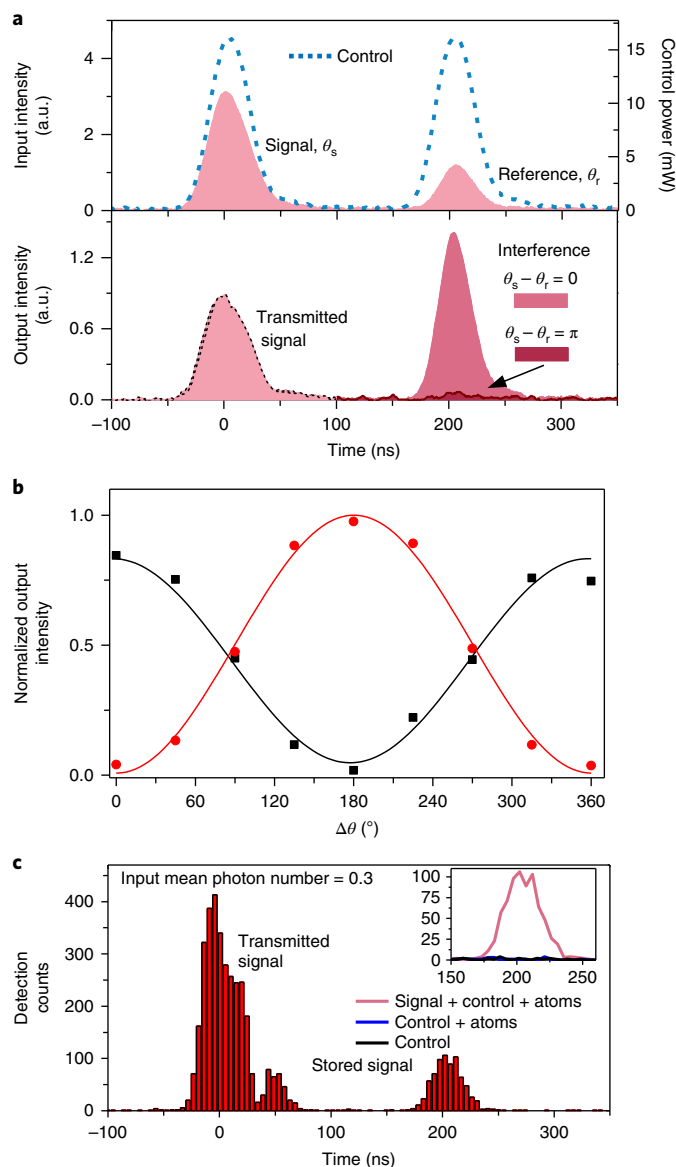
Fig. 4 | Phase preservation and single-photon level operation. a, Signal pulse with variable phase θ_s is stored and retrieved after 200 ns. At the moment of recall, a reference pulse with a fixed phase θ_r is sent to the medium (upper panel). The transmitted portion of the reference pulse and recalled signal pulse interfere with an intensity that depends on the difference between θ_s and θ_r. Two such interference measurements are illustrated in the lower panel for $\Delta\theta = \theta_s - \theta_r = 0$ and $\Delta\theta = \pi$, as detailed in Supplementary Section 2. **b,** θ_s is varied from 0° to 360° in steps of 45° and the resulting intensity measurements (I) yield an interference visibility $V = (I_{max} - I_{min})/(I_{max} + I_{min}) = 89 \pm 6\%$ and $V = 98 \pm 2\%$ for additional phase of 0 (black squares) and π (red circles) introduced by the control fields, respectively. Each dataset is fit to a sinusoidal function. **c,** Time-resolved photon detection histogram for storage and recall of signal pulses containing 0.3 photon on average, obtained after 10^5 trials. The memory efficiency is reduced to $\approx 5\%$ due to spatial mismatch between the signal and control with large separation angle. The inset shows measurement results for three configurations to evaluate noise contribution for the same number of trials: signal on/control on/MOT on (red), signal off/control on/MOT on (blue), and signal off/control on/MOT off, see Supplementary Section 2 for details.

As described above, optimal writing requires a control area $A_c^{write}(\tau) = \int_0^\tau \Omega_c(t)dt = 2\pi$, where $\tau \propto 1/B_{FWHM}$ is the input signal duration that temporally overlaps with the write field. Increasing

the bandwidth of an ATS memory (decreasing τ) requires increasing $\Omega_c(t) \propto \sqrt{\mathcal{P}}$. To demonstrate this feature, we first measure the memory efficiency as a function of the write pulse area, verifying that optimal pulse area for the write is 2π (Fig. 5a). Next, we increase the bandwidth of the input signal from $B_{FWHM} = 11$ MHz ($\tau_{FWHM} = 40$ ns) to $B_{FWHM} \approx 14.7$ MHz ($\tau_{FWHM} = 30$ ns). Accordingly, we decrease the duration of the write pulse to 30 ns (at FWHM), and increase its peak power from $\mathcal{P}_{peak} = 8.5$ mW to 15 mW to maintain the pulse area at 2π (Fig. 5b). After 200 ns storage, retrieval is achieved via a read-out pulse with the same profile as the write, resulting in memory efficiency of $\eta^{exp} = 8.4\%$.

Temporal compression and stretching. The pulse-area-based operation of an ATS memory can be used for manipulating the temporal profile of optical pulses. As in the writing process, optimal read-out requires the pulse area $A_c^{read}(\tau) = 2\pi$, which we experimentally confirm by measuring the storage efficiency versus read-out pulse area (Fig. 5a). In contrast, the read-out pulse duration does not need to match the input signal's duration. Provided that $\Omega_c(t)$ is set to give $A_c^{read}(\tau) = 2\pi$, the read-out can be longer or shorter than the input, leading to temporally stretched or compressed output signals, respectively. To demonstrate this, we store a $\tau_{FWHM} = 60$ ns (or $\tau_{FWHM} = 30$ ns) signal pulse using a 60 ns (or 30 ns) write pulse, but retrieve it using a 30 ns (or 60 ns) read-out pulse, leading a temporally compressed (or stretched) output by a compression (stretching) factor of 2, as shown in Fig. 5c (Fig. 5d). This pulse-shaping capability may be used for bandwidth matching between different photonic and atomic systems[21,47].

Temporal beam-splitting. Finally, we demonstrate that an ATS memory can serve as a network of reconfigurable 2×2 temporal beam-splitters that have arbitrary splitting ratios and phase control. In this scheme, the spin-wave mode and photonic mode are analogous to the input and output ports of the ATS temporal beam-splitter. Each control pulse (write or read-out) functions as a beam-splitter, performing a unitary transformation of the coherence between the input and output ports. The pulse area, from zero to 2π, determines the splitting ratio between the photonic mode (retrieved or transmitted) and the spin mode. In this way, the coherence of an input photonic mode can be mapped onto the spin-wave modes and output photonic modes with desired fractions using one or more control pulses (beam-splitters) with appropriate pulse areas, as experimentally demonstrated in Fig. 6. In these measurements, the initial coherence from the input photonic mode is recalled in one, two or four distinct temporal modes with nearly equal amplitudes, as illustrated in Fig. 6a–c, respectively.

The temporal beam-splitting operation of the ATS memory can be used for interfering optical signals from distinct temporal modes, suitable for a time-domain version of Hong–Ou–Mandel interference, or manipulation of time-bin photonic qubits. To demonstrate this (Fig. 6d), two control fields are used to map coherence from two equal-amplitude time-separated input photonic modes (E_1^{in} and E_2^{in}, with phases of θ_1 and θ_2, respectively) onto two equal-amplitude spin modes (S_1 and S_2) that interfere in the medium. The coherence from the interfering spin-waves is converted back into a single output photonic mode, whose amplitude depends on the relative phase of the input modes. Such atom-mediated photonic interference via an ATS memory, which is of probabilistic nature as in optical counterparts—but much more robust—can be broadly useful in quantum communication and optical quantum computing[41,47–49].

Discussion

The ATS memory protocol combines favourable features from other memory techniques in a single implementation, which relaxes the technical requirements for broadband quantum memories, as further detailed in Methods and Supplementary Section 7.
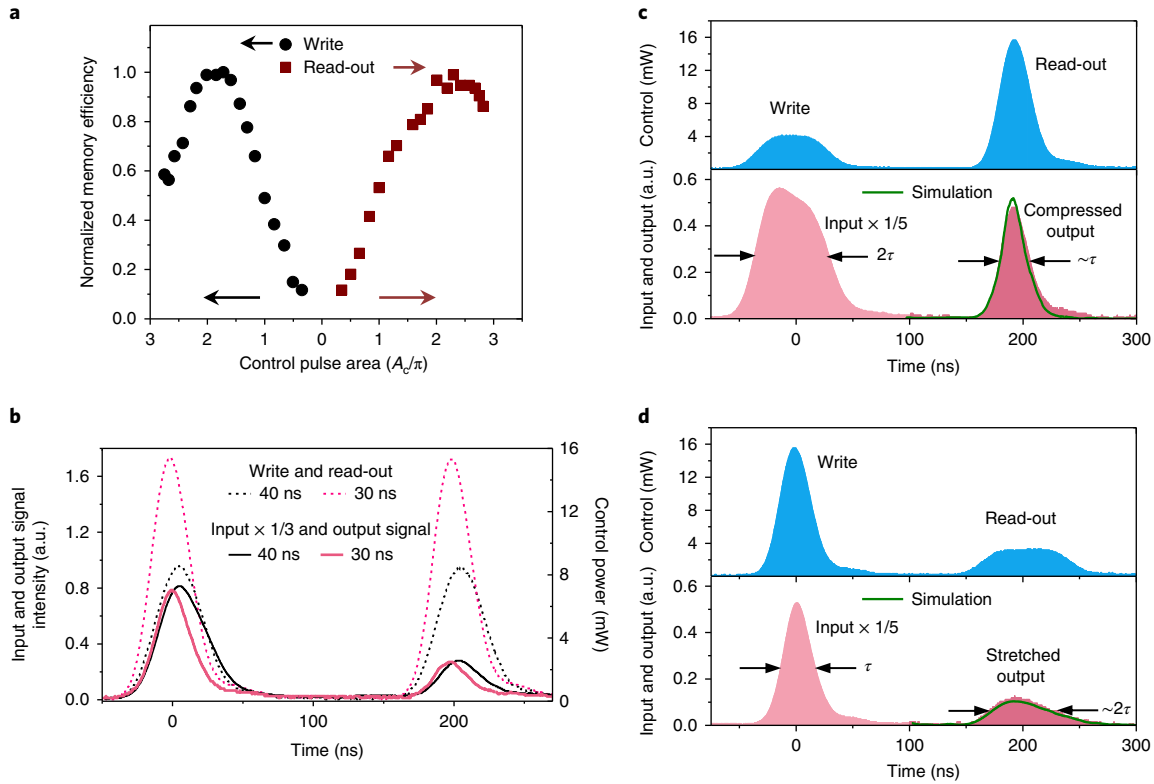
Fig. 5 | Dynamic control of memory bandwidth and temporal shaping of signal pulses. a, The memory efficiency with respect to write pulse area (A_c^{write}) and read-out pulse area (A_c^{read}), each with the same profile as the input signal, is independently characterized for storage of a Gaussian signal pulse with $\tau_{FWHM} = 40$ ns. For each pulse-area setting, the required peak Rabi frequency and peak power are calculated from $A_c(\tau) = \Omega_c^{peak}\sqrt{\pi/(2\ln2)}\,\tau_{FWHM}$ and $P_c^{peak} = (\Omega_c^{peak}/\alpha)^2$, where $\alpha/2\pi = 5.75\,MHz/\sqrt{mW}$ (Fig. 3c). **b**, The dynamic control of the acceptance bandwidth is demonstrated for 11.0 MHz and 14.7 MHz input signals ($\tau_{FWHM} = 40$ ns and $\tau_{FWHM} = 30$ ns) using write/read-out control pulses with peak powers of 8.5 mW and 15.0 mW, respectively, such that $A_c^{write} = 2\pi$. After 200 ns storage, recalled signals with efficiencies of 8.8% and 8.4% are measured for the 11 MHz and 14.7 MHz bandwidths, respectively. **c,d**, Temporal compression (**c**) (stretching (**d**)) of an input signal pulse with $\tau_{FWHM} = 60$ ns ($\tau_{FWHM} = 30$ ns) is demonstrated. This is accomplished by storing the signal with a write control pulse of the same duration as the signal input and $A_c^{write} = 2\pi$, but retrieving it using a read-out pulse of shorter (longer) duration than the input while maintaining $A_c^{read} = 2\pi$. The output is a compressed (stretched) pulse with $\tau_{FWHM} = 28$ ns ($\tau_{FWHM} = 58$ ns) and $\eta^{exp} = 7.4\%$ (8.6%), yielding about a factor of 2 compression (stretching). The experimental results are well simulated using the parameters of $d^{exp} = 3.5$, $\Gamma^{exp}/2\pi = 7.7$ MHz and $\gamma_s^{exp}/2\pi = 0.35$ MHz, as shown by solid green lines.

Similar to the EIT scheme[50], ATS memory is an on-resonant interaction scheme that benefits from large light–matter coupling. Yet, ATS memory also resembles the far-off-resonant Raman scheme[23,51], featuring dynamically controlled absorption and bandwidth. Despite these similarities, the physical process behind the ATS scheme is fundamentally different from both of these protocols. The EIT and Raman schemes rely on the adiabatic elimination of the atomic polarization (that is elimination of absorption through excited level, $|e\rangle$), which requires fulfilling the 'adiabaticity' condition[39],

$$d\tau\gamma_e \gg 1 \qquad (8)$$

whereas the ATS scheme relies on the excitation of the atomic polarization which requires 'fast' operation in the regime

$$d\tau\gamma_e \sim 1 \qquad (9)$$

This fundamental distinction leads to substantially different optimal operation requirements for storage and retrieval of broadband pulses ($B \gg \Gamma/2\pi$). For a given short signal pulse with $\tau \ll 1/\gamma_e$, optimally efficient storage can be achieved in the ATS scheme for optical depths 5 to 10 times smaller than for adiabatic memories, as presented in Fig. 2c. Equivalently, for a given d and γ_e, the optimal

efficiency can be achieved in the ATS scheme with signal pulses 5 to 10 times shorter than for adiabatic memories, as shown in Fig. 2d. Furthermore, in contrast to the optical depth dependent 'shape' optimization of the control field required in the EIT and Raman schemes[40,51,52], the ATS approach features 'pulse area' optimization with substantially smaller control power (inset of Fig. 2d), which reduces technical complexity and simplifies the optimization procedure significantly.

Being a non-adiabatic memory, the absorption and high-speed pulse-area-based operation of the ATS protocol exhibits the same character and efficiency scaling of the photon-echo memory techniques[43], including controlled reversible inhomogeneous broadening (CRIB)[53–55], gradient echo memory (GEM)[56] and atomic frequency comb (AFC)[42] protocols. Moreover, as will be detailed in a forthcoming manuscript, ATS memory shares a favourable multimode storage scaling with the CRIB/GEM protocols, which has linear dependence on optical depth, in contrast to the quadratic dependence of EIT and Raman memories[57]. Despite these common features, the ATS protocol needs neither electric- nor magnetic-field-controlled absorption mechanisms like CRIB/GEM protocols, nor preparation of absorption lines via persistent-hole burning techniques like the AFC scheme. Instead, ATS memory relies on the a.c. Stark splitting of an absorption line, featuring all-optical control, which is technically much less demanding and more versatile
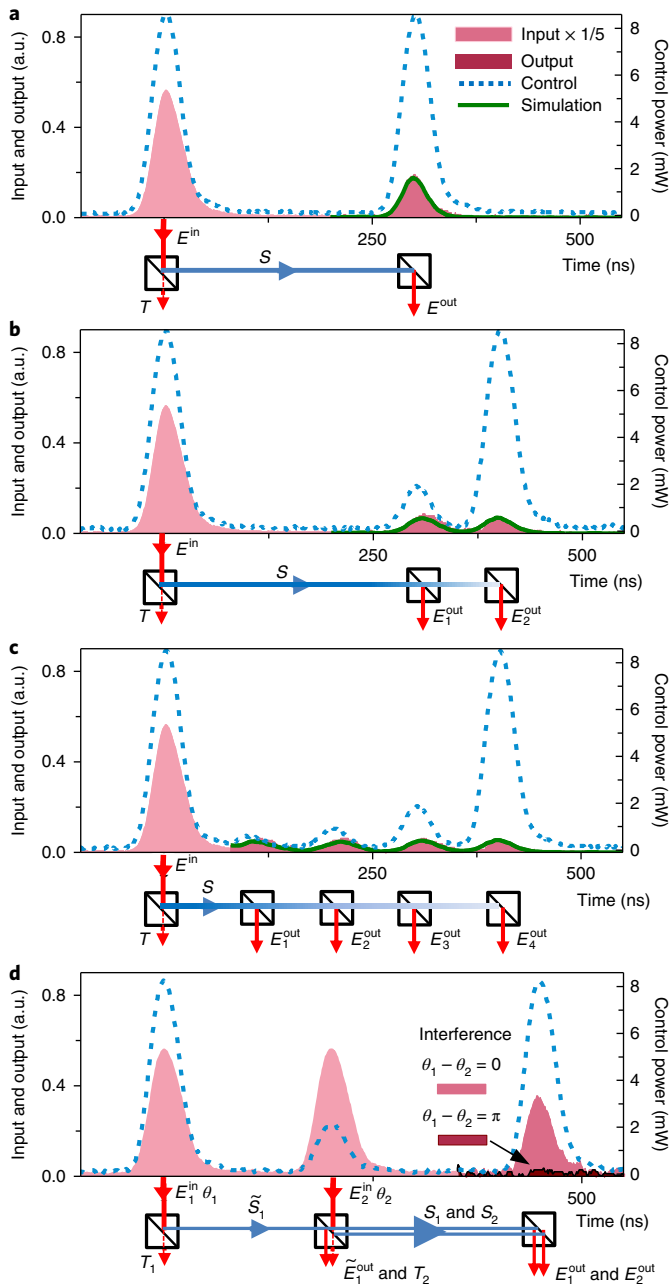
Fig. 6 | Demonstration of temporal-beam-splitting. a–c, Coherence from input photonic mode E^{in} is partially mapped onto spin-wave mode S and transmitted photonic mode T (due to non-unity absorption probability in our memory) using a write control pulse with $A_c = 2\pi$. The stored coherence in S is transformed back to a single (E^{out}) (**a**), two (E_1^{out} and E_2^{out}) (**b**) or four (E_1^{out}, E_2^{out}, E_3^{out}, E_4^{out}) (**c**) output photonic modes using one, two or four read-out control pulses with appropriately selected areas ($\leq 2\pi$), respectively. The experimental results are well simulated by using $d^{exp} = 3.5$, $\gamma_s^{exp}/2\pi = 0.32$ MHz and $\Gamma^{exp}/2\pi = 7.7$ MHz (green solid lines). **d**, Two-mode interference. Coherence from two distinct input photonic modes E_1^{in} and E_2^{in} with phases θ_1 and θ_2, is mapped onto two spin-wave modes in the same storage medium, $\tilde{S}_1$ and S_2, using the control pulses with the same phase and areas of 2π and π, respectively. After the second control pulse, the resulting spin-waves S_1 and S_2 interfere with equal amplitudes. The third control pulse transforms coherence from the interfering spin-waves to an output photonic mode whose intensity depends on ($\theta_1 - \theta_2$), as shown for $\Delta\theta = \theta_1 - \theta_2 = 0$ and $\Delta\theta = \pi$.

for broadband operation. With these intrinsic and technical advantages, the ATS memory scheme opens a new avenue for practical long-lived and broadband quantum memories.

For a direct experimental comparison of protocols, we evaluate the performance of the ATS protocol compared with EIT and off-resonant Raman approaches in our cold-atom system, featuring $\Gamma^{exp}/2\pi = 7.7$ MHz, $\gamma_s^{exp}/2\pi \approx 0.4$ MHz and $d^{exp} \approx 3.3$. First, we implement the off-resonant Raman scheme for storage of a signal with our typical bandwidth $B_{FWHM} = 11$ MHz, with a sufficiently large signal-control detuning from resonance ($\Delta \approx 3\Gamma$). After optimization we measure the memory efficiency of only $\approx 2\%$, which is significantly less than the typical efficiency of the ATS memory (7%) for the same storage time. This low efficiency is mainly due to insufficient coupling provided by our limited control power (particularly in the read-out stage), which prevents true adiabatic operation with the given short signal pulse. Second, we implement the EIT-based slow-light scheme, which necessitates narrowing the signal bandwidth to satisfy the adiabaticity condition with our low optical depth. Although we observe a group delay of ≈ 70 ns for a signal field with $B_{FWHM} \approx 1.2$ MHz bandwidth ($\tau_{FWHM} = 380$ ns), it is not possible to completely stop this signal for storage/retrieval because of the large spin decoherence rate in our system. For further verification, we analyse numerically the optimal efficiency of the ATS and EIT memories as a function of the spin-decoherence rate in our experimental regime, as shown in Fig. 2e. Our results demonstrate exceptional robustness of the ATS memory against spin decoherence, indicating the possibility for implementing photon storage and manipulation in three-level systems where EIT cannot be observed.

In conclusion, we have introduced and experimentally demonstrated a novel light storage and manipulation technique based on dynamically controlled ATS. Our approach is inherently suitable for the realization of high-speed quantum optical devices in variety of atomic and molecular systems. We anticipate that our investigation will spur further fundamental studies and will bring new possibilities in precision spectroscopy, metrology and quantum information.

Online content

Any methods, additional references, Nature Research reporting summaries, source data, statements of data availability and associated accession codes are available at https://doi.org/10.1038/s41566-018-0279-0.

References

1. Autler, S. H. & Townes, C. H. Stark effect in rapidly varying fields. *Phys. Rev.* **100**, 703–722 (1955).
2. Picque, J. L. & Pinard, J. Direct observation of the Autler–Townes effect in the optical range. *J. Phys. B* **9**, L77–L81 (1976).
3. He, X. F., Fisk, P. T. H. & Manson, N. B. Autler–Townes effect of the photoexcited diamond nitrogen-vacancy center in its triplet ground state. *J. Appl. Phys.* **72**, 211–217 (1992).
4. Zhu, Y. F. et al. Vacuum Rabi splitting as a feature of analysis and experimental-observations. *Phys. Rev. Lett.* **64**, 2499–2502 (1990).
5. Thompson, R. J., Rempe, G. & Kimble, H. J. Observation of normal-mode splitting for an atom in an optical cavity. *Phys. Rev. Lett.* **68**, 1132–1135 (1992).
6. Bernadot, F., Nussenzveig, P., Brune, M., Raimond, J. M. & Haroche, S. Vacuum Rabi splitting observed on a microscopic atomic sample in a microwave cavity. *Europhys. Lett.* **17**, 33–38 (1992).
7. Wade, C. G. et al. Probing an excited-state atomic transition using hyperfine quantum-beat spectroscopy. *Phys. Rev. A* **90**, 033424 (2014).
8. Holloway, C. L. et al. Sub-wavelength imaging and field mapping via electromagnetically induced transparency and Autler–Townes splitting in Rydberg atoms. *App. Phys. Lett.* **104**, 244012 (2014).
9. Ghafoor, F. Autler–Townes multiplet spectroscopy. *Laser. Phys.* **24**, 035702 (2014).

10. Lukin, M. D. Colloquium: trapping and manipulating photon states in atomic ensembles. *Rev. Mod. Phys.* **75**, 457–472 (2003).
11. Fleischhauer, M., Imamoglu, A. & Marangos, J. P. Electromagnetically induced transparency: optics in coherent media. *Rev. Mod. Phys.* **77**, 633–673 (2005).
12. Abi-Salloum, T. Y. Electromagnetically induced transparency and Autler-–Townes splitting: two similar but distinct phenomena in two categories of three-level atomic systems. *Phys. Rev. A* **81**, 053836 (2010).
13. Anisimov, P. M., Dowling, J. P. & Sanders, B. C. Objectively discerning Autler–Townes splitting from electromagnetically induced transparency. *Phys. Rev. Lett.* **107**, 163604 (2011).
14. Giner, L. et al. Experimental investigation of the transition between Autler–Townes splitting and electromagnetically-induced-transparency models. *Phys. Rev. A* **87**, 013823 (2013).
15. Tan, C. & Huang, G. Crossover from electromagnetically induced transparency to Autler–Townes splitting in open ladder systems with Doppler broadening. *J. Opt. Soc. Am. B* **31**, 704–715 (2014).
16. Peng, B., Chen, W., Nori, F., Ozdemir, K. O. & Yang, L. What is and what is not electromagnetically induced transparency in whispering-gallery microcavities. *Nat. Commun.* **5**, 5082 (2014).
17. Lu, X. et al. Transition from Autler–Townes splitting to electromagnetically induced transparency based on the dynamics of decaying dressed states. *J. Phys. B* **48**, 055003 (2015).
18. He, L.-Y., Wang, T.-J., Gao, Y.-P., Cao, C. & Wang, C. Discerning electromagnetically induced transparency from Autler–Townes splitting in plasmonic waveguide and coupled resonators system. *Opt. Express* **23**, 23817–23826 (2015).
19. Liao, W.-T., Keitel, C. H. & Pálffy, A. All-electromagnetic control of broadband quantum excitations using gradient photon echoes. *Phys. Rev. Lett.* **113**, 123602 (2014).
20. Liu, C., Dutton, Z., Behroozi, C. H. & Hau, L. V. Observation of coherent optical information storage in an atomic medium using halted light pulses. *Nature* **409**, 490–493 (2001).
21. Hosseini, M. et al. Coherent optical pulse sequencer for quantum applications. *Nature* **461**, 241–245 (2009).
22. Afzelius, M. et al. Demonstration of atomic frequency comb memory for light with spin-wave storage. *Phys. Rev. Lett.* **104**, 040503 (2010).
23. Reim, K. F. et al. Towards high-speed optical quantum memories. *Nat. Photon.* **4**, 218–221 (2010).
24. Hedges, M. P., Longdell, J. J., Li, Y. & Sellars, M. J. Efficient quantum memory for light. *Nature* **465**, 1052–1056 (2010).
25. Clausen, C. et al. Quantum storage of photonic entanglement in a crystal. *Nature* **469**, 508–512 (2011).
26. Saglamyurek, E. et al. Broadband waveguide quantum memory for entangled photons. *Nature* **469**, 513–518 (2011).
27. Mohapatra, A. K., Jackson, T. R. & Adams, C. S. Coherent optical detection of highly excited Rydberg states using electromagnetically induced transparency. *Phys. Rev. Lett.* **98**, 113003 (2007).
28. Pritchard, J. D. et al. Cooperative atom–light interaction in a blockaded Rydberg ensemble. *Phys. Rev. Lett.* **105**, 193603 (2010).
29. Zhou, Y. et al. Coherent control of a strongly driven silicon vacancy optical transition in diamond. *Nat. Commun.* **8**, 14451 (2017).
30. Siyushev, P. et al. Optical and microwave control of germanium-vacancy center spins in diamond. *Phys. Rev. B* **96**, 081201(R) (2017).
31. Agarwal, G. S. & Huang, S. Electromagnetically induced transparency in mechanical effects of light. *Phys. Rev. A* **81**, 041803 (2010).
32. Huang, J. Y. et al. In situ observation of the electrochemical lithiation of a single SnO$_2$ nanowire electrode. *Science* **330**, 1515–1520 (2010).
33. Teufel, J. D. et al. Circuit cavity electromechanics in the strong-coupling regime. *Nature* **471**, 204–208 (2011).
34. Safavi-Naeini, A. H. et al. Electromagnetically induced transparency and slow light with optomechanics. *Nature* **472**, 69–73 (2011).
35. Sillanpää, M. A. et al. Autler–Townes effect in a superconducting three-level system. *Phys. Rev. Lett.* **103**, 193601 (2009).
36. Abdumalikov, A. A. et al. Electromagnetically induced transparency on a single artificial atom. *Phys. Rev. Lett.* **104**, 193601 (2010).
37. Novikov, S. et al. Autler–Townes splitting in a three-dimensional transmon superconducting qubit. *Phys. Rev. B* **88**, 060503 (2013).
38. Sun, H.-C. et al. Electromagnetically induced transparency and Autler–Townes splitting in superconducting flux quantum circuits. *Phys. Rev. A* **89**, 063822 (2014).
39. Gorshkov, A. V., André, A., Sørensen, A. S. & Lukin, M. D. Universal approach to optimal photon storage in atomic media. *Phys. Rev. Lett.* **98**, 123601 (2007).
40. Gorshkov, A. V., André, A., Lukin, M. D. & Sørensen, A. S. Photon storage in Λ-type optically dense atomic media. II. Free-space model. *Phys. Rev. A* **76**, 033804 (2007).

41. Heshami, K. et al. Quantum memories: emerging applications and recent advances. *J. Mod. Opt.* **63**, 2005–2028 (2016).
42. Afzelius, M., Simon, C., de Riedmatten, H. & Gisin, N. Multimode quantum memory based on atomic frequency combs. *Phys. Rev. A* **79**, 052329 (2009).
43. Tittel, W. et al. Photon-echo quantum memory in solid state system. *Laser Photon. Rev.* **4**, 244–267 (2010).
44. Riedl, S. et al. Bose–Einstein condensate as a quantum memory for a photonic polarization qubit. *Phys. Rev. A* **85**, 022318 (2012).
45. Cho, Y.-W. et al. Highly efficient optical quantum memory with long coherence time in cold atoms. *Optica* **3**, 100–107 (2016).
46. Hsiao, Y.-F. et al. Highly efficient coherent optical memory based on electromagnetically induced transparency. *Phys. Rev. Lett.* **120**, 183602 (2018).
47. Saglamyurek, E. et al. An integrated processor for photonic quantum states using a broadband light–matter interface. *New J. Phys.* **16**, 065019 (2014).
48. Reim, K. F. et al. Multipulse addressing of a raman quantum memory: configurable beam splitting and efficient readout. *Phys. Rev. Lett.* **108**, 263602 (2013).
49. Campbell, G. T. et al. Configurable unitary transformations and linear logic gates using quantum memories. *Phys. Rev. Lett.* **113**, 063601 (2014).
50. Lukin, M. D. & Imamoglu, A. Controlling photons using electromagnetically induced transparency. *Nature* **413**, 273–276 (2001).
51. Nunn, J. et al. Mapping broadband single-photon wave packets into an atomic memory. *Phys. Rev. A* **75**, 011401(R) (2007).
52. Novikova, I., Phillips, N. B. & Gorshkov, A. V. Optimal light storage with full pulse-shape control. *Phys. Rev. A* **78**, 021802(R) (2008).
53. Nillson, M. & Kroll, S. Solid-state quantum memory using complete absorption and re-emission of photons by tailored and externally controlled inhomogeneous absorption profiles. *Opt. Commun.* **247**, 393–403 (2005).
54. Alexander, A. L., Longdell, J. J., Sellars, M. J. & Manson, N. B. Photon echoes produced by switching electric fields. *Phys. Rev. Lett.* **96**, 043602 (2006).
55. Kraus, J. B. et al. Quantum memory for nonstationary light fields based on controlled reversible inhomogeneous broadening. *Phys. Rev. A* **73**, 020302(R) (2006).
56. Hetet, G., Longdell, J. J., Alexander, A. L., Lam, P. K. & Sellars, M. J. Electro-optic quantum memory for light using two-level atoms. *Phys. Rev. Lett.* **100**, 023601 (2008).
57. Nunn, J. et al. Multimode memories in atomic ensembles. *Phys. Rev. Lett.* **101**, 260502 (2008).

Acknowledgements

Author contributions

The ATS memory approach was proposed by E.S. with feedback from K.H. and L.J.L. The project was supervised by L.J.L. and E.S. The ultracold atom apparatus was designed by L.J.L., and it was built and commissioned by L.J.L., T.H. and E.S. The design of the experiments, the measurements and the analysis of the results were performed by E.S. and T.H. The numerical modelling of the ATS memory was performed by K.H. with input from E.S. The simulations and numerical analysis were performed by E.S. and A.R. with the guidance of K.H. The manuscript was written by E.S. and L.J.L. with feedback from all co-authors.

Competing interests

The authors declare no competing interests.

Additional information

Methods

ATS memory efficiency. We define the total memory efficiency η to be the ratio of the number of photons in the output mode ($\propto |E(L, t > T)|^2$, where T is the storage time) to the number of photons in the input mode ($\propto |E(0, t < \tau)|^2$, where τ is the pulse duration). As in the general case for spin-wave storage, this efficiency is determined by three factors[40]: (1) the storage efficiency η_s, given by the ratio of the number of stored spin excitations to the number of incoming photons; (2) the retrieval efficiency η_r, given by the ratio of the number of retrieved photons to the number of stored spin excitations; (3) the spin-wave survival efficiency during storage η_d, which is determined by decoherence effects that arise in practical settings. Together, the overall efficiency is the product of these three

$$\eta = \frac{\int_T^\infty |E(L,t)|^2 \, dt}{\int_0^\tau |E(0,t)|^2 \, dt} = \eta_s \eta_r \eta_d \tag{10}$$

In the ATS memory, the reversible transfer of coherence between the photonic and spin-wave modes is mediated by the evolution of the coherence onto the collective state between $|e\rangle$ and $|g\rangle$, which describes the polarization mode. In the writing stage, the initial coherence from the input photonic mode is mapped onto the polarization (the absorption process) that simultaneously begins its evolution to the spin-wave mode (as per equations (5)–(7)), and initiates storage. Thus the storage efficiency η_s depends on two factors: first, the absorption factor μ_{abs} is the coherent sum of the absorption probabilities of the input photonic excitation by each atom in the ensemble (determined by d, Ω_c^{write} and Γ); second, μ_w is the efficiency of the polarization-mediated reversible transfer between the photonic and the spin-wave modes (determined by $A_c^{write}(\Omega_c)$). When μ_w approaches unity, the number of excitations left in the polarization mode at the completion of the writing stage is minimal.

The same treatment can be applied for the read-out stage, in which coherence stored in the spin-wave mode is transferred to the polarization that simultaneously emits photons in the output mode (the re-emission process). In this case, the retrieval efficiency η_r depends on μ_{re}, the collective re-emission probability of the polarized atoms across the ensemble (determined by d, Ω_c^{read} and Γ), and μ_r, the efficiency of the polarization-mediated reversible transfer between the spin-wave and photonic modes (determined by $A_c^{read}(\Omega_c)$, in the same fashion as μ_w)

Using the terms stated above and assuming that spin-wave decoherence is negligibly small ($\eta_d \cong 1$), equation (10) is

$$\eta = \mu_w(A_c^{write}) \mu_{abs}(d, \Gamma, \Omega_c^{write}) \mu_{re}(d, \Gamma, \Omega_c^{read}) \mu_r(A_c^{read}) \tag{11}$$

In the particular case when the pulse area for both writing and read-out fields is $A_c^{write} = A_c^{read} = 2\pi$, no polarization remains in the medium right after the writing and reading, thereby achieving complete transfer of coherence between the photonic and spin-wave mode. Thus, μ_w and μ_r approach unity, and the memory efficiency simplifies to

$$\eta = \mu_{abs}\mu_{re} \tag{12}$$

which is solely determined by the collective absorption and re-emission processes. This description is common in resonant absorption-based quantum memory approaches, such as the AFC and CRIB protocols that have been well analysed[42,43]. The analytic solutions describing the memory efficiency for the forward-propagating mode (η_f) and backward-propagating mode (η_b) are

$$\eta_f = \tilde{d}^2 e^{-\tilde{d}} \mu_d \tag{13}$$

$$\eta_b = \left(1 - e^{-\tilde{d}}\right)^2 \mu_d \tag{14}$$

where $\tilde{d}$ and μ_d represent effective optical depth and collective-coherence survival probability for polarization (during writing and reading for ATS memory), respectively. Since the absorption and re-emission occur via ATS lines that span the signal spectrum B_{FWHM}, $\tilde{d}$ is an increasing function of peak optical depth (d) and the linewidth of the ATS peaks ($\Gamma/2$), and a decreasing function of the spacing between the ATS peaks ($\delta_A \approx \Omega_c$). Note that for the dynamic ATS cases, the effective peak spacing is equivalent to the peak spacing of the fixed ATS that provides the same pulse area. For $B_{FWHM} = \Omega_c/2\pi$ (equivalently $A_c^{write} = A_c^{read} = 2\pi$), the effective optical depth is given by $\tilde{d} = d/2F$ where $F = \Omega_c/\Gamma$ is the ATS factor. Decoherence (dephasing) of the polarization in the absorption and re-emission processes (which reduces μ_d) occurs due to the finite width of the ATS lines. Hence, μ_d is determined by the Fourier transform of an ATS line over the interaction time (input and output signal duration). This is equal to $e^{-1/F}$ for an ATS line, due to its Lorentzian lineshape. Using these definitions, the efficiency of the ATS memory under the specified conditions can be approximated as

$$\eta_f \approx (d/2F)^2 e^{-d/2F} e^{-1/F} \tag{15}$$

$$\eta_b \approx \left(1 - e^{-d/2F}\right)^2 e^{-1/F} \tag{16}$$

The efficiency results calculated from these expressions show reasonably good agreement with the numerically calculated efficiencies for a wide range of d and F, as presented in the main text with Fig. 2a,b. The inset of each figure illustrates the efficiency with respect to $\tilde{d}$, which provides additional insight together with equation (13) and (14). For the forward-propagating output mode and a given $F > 1$, the efficiency of the ATS memory increases until $\tilde{d} \approx 1.5$ (the optimal effective optical depth) as seen in Fig. 2a. In this regime, the first terms of equations (13) and (15) dominate because large optical depths (number of atoms) enhance the collective absorption and re-emission probability. As the optical depth is further increased, the efficiency decreases since the second exponentially decaying term dominates. This term effectively describes the re-absorption probability of the emitted photons, which are converted to the spin-wave excitation and remain in the medium after read-out. For this reason, the efficiency for the forward-propagating mode is limited to 54%, which is achieved when $\tilde{d} \approx 1.5$ and F is sufficiently large. In contrast, for the backward-propagating mode, the re-absorption term is eliminated due to the fact that constructively interfering re-emission occurs only at the input side of the medium. Thus, the efficiency is an always-increasing function of $\tilde{d}$ (first factor in equations (14) and (16)), and it tends to saturate for $\tilde{d} \gtrsim 3$, as seen in Fig. 2b. In addition to these factors, the efficiency strongly depends on the ATS factor F, which directly determines the polarization dephasing (the last term of equations (15) and (16)). In general for a given $\tilde{d}$, the total efficiency increases as F increases because of decreased polarization dephasing during the writing and read-out stages. Consequently, near-unity memory efficiency is possible with $F \gg 1$ and $\tilde{d} \gtrsim 3$ for the backward-propagating signal mode. It is worth emphasizing that although $F \approx 1$ and $F < 1$ are unfavourable ATS regimes (but favourable EIT regimes), the basic principle of our protocol will still work in a robust manner, but with non-optimal storage efficiency.

We note that in the near-optimal effective optical depth regime ($\tilde{d} \approx 1.5$ and 3.0 for the forward and backward recall, respectively), the maximum memory efficiency for a given Γ and signal field with B_{FWHM} is achieved only by control pulse areas $A_c^{write} = A_c^{read} = 2\pi$. However, this requirement is relaxed to some extent in the non-optimal effective optical depth regime, as can be inspected from equation (11) in conjuction with equations (13) and (14). When $\tilde{d}$ is significantly smaller than the optimal effective optical depth for both forward- and backward-propagating modes, a pulse area $A_c < 2\pi$ will lead to larger efficiency, as it effectively increases $\tilde{d}$ and yields larger $\mu_{abs}\mu_{re}$. However, at the same time, $A_c < 2\pi$ results in smaller $\mu_w\mu_r$. With this trade-off, the optimal efficiency can be found with pulse areas as small as $A_c = 1.6\pi$. Similarly, when $\tilde{d}$ is significantly larger than the optimal effective optical depth for the forward-propagating mode, the memory efficiency can be optimized by decreasing $\tilde{d}$ with pulse areas $A_c > 2\pi$. This leads to a compromise between the increase of $\mu_{abs}\mu_{re}$ and decrease of $\mu_w\mu_r$ such that the efficiency can be maximized away from $A_c = 2\pi$. In contrast, for the backward recall in the large effective optical depth regime ($\tilde{d} > 3$), the maximum efficiency is always obtained at $A_c = 2\pi$, as larger optical depths are favourable in this configuration.

Finally, for evaluation of the performance of the ATS scheme on the basis of the universal picture of quantum memory approaches discussed by Gorshkov et al.[39], it is useful to rephrase our optimal operation conditions, derived as $F = \Omega_c/\Gamma \gg 1$ and $\tilde{d} = d/2F \approx 3$ for the backward retrieval scheme in terms of d, τ and γ_e. As the relationship between the signal bandwidth ($B_{FWHM} \approx 0.5/\tau_{FWHM}$) and the peak Rabi frequency (Ω_c) in our protocol is given by $B_{FWHM} \approx \Omega_c/2\pi$, the condition of $F \gg 1$ is equivalent to $\tau_{FWHM} \ll 1/\gamma_e$ (recall that $\gamma_e = \Gamma/2$). Similarly, using these definitions, the condition of $\tilde{d} \approx 3$ translates into the condition $d\tau_{FWHM}\gamma_e \approx 8$ for optimal efficiency, and $1 < d\tau_{FWHM}\gamma_e < 8$ for reasonably large efficiencies compared with adiabatic memories (see Fig. 2a–c). The generalization of these bounds for non-Gaussian pulses yields

$$\tau \ll 1/\gamma_e \quad \text{and} \quad d\tau\gamma_e \sim 1 \tag{17}$$

which puts ATS memory into the category of non-adiabatic or fast memory, as will be further discussed.

Optical-depth requirement for broadband memory. The efficiencies of all memory protocols follow a certain functional form, parameterized by optical depth and protocol-specific parameters such as the ATS factor (F) for ATS memory, fractional signal delay (T_{delay}/τ) for EIT and signal-control detuning (Δ) for off-resonant Raman memory. Optical depth is the universal parameter that sets the maximally achievable efficiency (optimal efficiency) independent of memory protocol. Memory protocols have different requirements and operational conditions to reach the same optimal efficiency. For adiabatic memory protocols such as EIT and Raman, optimal efficiency is achieved by fulfilling $d\tau\gamma_e \gg 1$ that leads to adiabatic elimination of the atomic polarization. In contrast, for fast memory protocols such as the ATS and photon-echo schemes, optimal efficiency is achieved by $d\tau\gamma_e \sim 1$ that leads to maximizing atomic polarization in storage/retrieval stages. In this situation, for a given d and γ_e, the fast memory protocols can operate with at least 5–10 times shorter pulse duration than adiabatic memory protocols for equally efficient storage (Fig. 2d). Equivalently, efficient storage of

short pulses (such that $B_{FWHM} \gg \Gamma/2\pi$) via fast memories relaxes the optical depth requirement about 5–10 times with respect to adiabatic memories (Fig. 2c).

Following a treatment similar to that of Gorshkov et al.[40], we have verified numerically the optimal operation regimes of adiabatic and fast memories by analysing EIT/Raman and ATS protocols, respectively. First, for a consistency check, we show that for storage and retrieval of a long pulse $\tau_{FWHM} \approx 20/\gamma_e$ (≈ 1-μs-long pulse in our Rb system) via the EIT protocol (as an adiabatic memory), optimal efficiency can be obtained for a wide range of optical depth values ($d \geq 2$) by satisfying $d\tau_{FWHM}\gamma_e > 40$ together with optimized shapes of the control field, as shown with the dashed curve in Fig. 2c, which agrees with previous work[39,40]. Next, we investigate the limit of the adiabaticity condition for both EIT and off-resonant Raman memory for storage and recall of a short pulse $\tau_{FWHM} \ll 1/\gamma_e = 0.1/\gamma_e$ (≈ 5.4-ns-long pulse in our system) with optimized parameters (Ω_c and Δ) and control field shape, as further detailed in Supplementary Section 7. We find that at $d \approx 400$–600, near-optimal efficiency is reached for both schemes, which provides $d\tau_{FWHM}\gamma_e \approx 40$–60, similar to previous results[40]. Below this regime, the adiabaticity condition breaks down, leading to non-optimal efficiency. We perform the same analysis for the ATS protocol and find that significantly larger memory efficiency (compared with adiabatic memories) can be obtained with $d < 100$ (in the regime of $1 < d\tau_{FWHM}\gamma_e < 10$), approaching the optimal efficiency at $d \approx 80$–100 which satisfies $d\tau_{FWHM}\gamma_e \approx 8$–10. In addition, we show that optimal efficiency of the ATS memory for any optical depth can be achieved simply by providing the signal duration $\tau_{FWHM} \approx 10/d\gamma_e$, which is illustrated with the same dashed line in Fig. 2c. To conclude our investigation, we analyse the bandwidth scaling of ATS and EIT/Raman memories as a function of optical depth under optimal conditions. We verified numerically that as the signal bandwidth ($B_{FWHM} \gg \gamma_e/2\pi$) is increased away from the optimal bandwidth, optical depth needs to be increased proportionally to maintain the limit adiabatic ($d\tau_{FWHM}\gamma_e \approx 50 \pm 10$) and the fast operation ($d\tau_{FWHM}\gamma_e \approx 8$) conditions, and hence optimal efficiency, for EIT/Raman and ATS memories, respectively, as shown in Fig. 2d. This favourable scaling of the ATS memory substantially reduces the demand on optical depth for practical implementation of broadband light storage. For example, efficient storage of subnanosecond pulses in Rb on the D1 line ($B_{FWHM} \approx 100\Gamma/2\pi$) would require optical depth of a few thousand using the EIT or off-resonant Raman scheme, but only a few hundred using the ATS scheme.

Control power and optimization requirements for broadband memory. Another important benchmark for spin-wave memories is the strength of the control field (Rabi frequency, $\Omega_c \propto \sqrt{\mathcal{P}}$) required for optimal efficiency. It is important to implement storage with small Ω_c (peak Rabi frequency) to relax the demands on large control power, and to reduce the complexity of spectral and spatial filtering of the control field from the signal field. Furthermore, fundamental issues, such as four-wave mixing noise, which cannot be eliminated by the standard filtering techniques, become severe with large control power[58,59]. Therefore, providing optimal memory operation with small Ω_c is also highly desirable for minimizing this effect.

ATS memory and photon-echo memories have certain Rabi frequency requirements, imposed by the optimum pulse areas of 2π and π, respectively. For ATS memory under the optimal pulse area condition ($A_c \approx 2\pi$), the required peak Rabi frequency for efficient storage of a signal with B_{FWHM} is given by $\Omega_c/2\pi \approx B_{FWHM}$, which essentially optimizes the signal absorption. In contrast, in the EIT and Raman protocols, the strength and shape of the control field need to be optimized for the adiabatic elimination of the absorption through the excited level. For the EIT scheme, this condition translates into $B_{FWHM} < B_{EIT} < \Omega_c/2\pi$, where B_{EIT} is the EIT transparency window. Specifically, in the broadband operation regime ($B_{FWHM} \gg \Gamma/2\pi$), where the slow-light effect is mediated by the dispersion due to ATS lines (instead of an EIT dip in the transition line), this condition ideally requires that ATS splitting ($\delta_{ATS}/2\pi = \Omega_c/2\pi$) is significantly wider than the signal bandwidth. Consequently, for a given signal bandwidth with $B_{FWHM} \gg \Gamma/2\pi$, the optimal operation of EIT memory requires optimal peak Rabi frequency to be $\Omega_c/2\pi > B_{FWHM}$, compared with $\Omega_c/2\pi \approx B_{FWHM}$ for ATS memory. We numerically verify that due to this condition, the EIT scheme requires at least four-times larger peak power (two-times larger peak Rabi frequency) than the ATS scheme, as shown in the inset of Fig. 2d.

A similar bound on the optimal peak Rabi frequency can be derived for the off-resonant Raman protocol, which requires $\Delta \gg \gamma_e$ to eliminate spontaneous emission (absorption through $|e\rangle$). As described previously[40,51], this approach is unlike other protocols in that the peak Rabi frequency Ω_c directly increases coupling to the signal field (effective coupling), given by $C = \sqrt{W}\sqrt{d\gamma_e}/\Delta$, where $\sqrt{d\gamma_e}$ and $\sqrt{W}$ are the matter-coupling component and light-coupling component with $W \sim \Omega_c^2/B_{FWHM}$ (control pulse energy), respectively. This feature is particularly crucial in the long-pulse storage regime, which allows optimal efficiency to be reached by compensating weak coupling due to far-off-resonant operation. However, in the short-pulse storage regime ($B_{FWHM} \gg \Gamma/\pi$), as analysed by Nunn et al.[51], W cannot be arbitrarily increased as a function of Ω_c to enhance effective coupling C, since the condition $\Omega_c < \Delta$ also needs to be met as another requirement for adiabaticity. For optimal storage efficiency, the effective coupling needs to be $C \sim 1$ with $\sqrt{W} \sim \sqrt{d\gamma_e} \sim \Delta$, which provides a balance between the light and matter coupling components. This condition imposes a

bound on the peak Rabi frequency as $\Omega_c \sim \sqrt{B_{FWHM}d\gamma_e}$. Combining this limit with the general adiabaticity condition ($B_{FWHM} \ll d\gamma_e$) implies the optimal peak Rabi frequency to be $\Omega_c/2\pi > B_{FWHM}$, compared with the bound of ATS memory given by $\Omega_c/2\pi \approx B_{FWHM}$. We numerically verified that due to this condition, the optimal storage with the Raman scheme requires at least four-times larger control power (twice-larger Rabi frequency) compared to the ATS scheme for the same bandwidth. Another important restriction with Raman memory in the short-pulse storage regime is that optimal retrieval can be achieved with read-out pulses that require about 2–3 times larger Rabi frequency than the writing Rabi frequency[51], as we confirm with our analysis shown in the inset of Fig. 2d. Hence, compared with ATS memory, this amounts 16–25 times larger read-out power, which is technically very challenging.

Finally, we point out that for adiabatic memories, the shaped-based optimization of the control field is necessary for optimal storage, whereas for fast memories, including ATS memory, the pulse-area-based operation is essential. As detailed in the previous theoretical and experimental studies for EIT and Raman memories[40,52], the determination of the optimal shape, which can vary from a simple ramp to complex mathematical profile depending on optical depth and the shape of input signal, requires the implementation of complicated algorithms[52]. However, in the ATS storage scheme, independent of optical depth, the use of a simple Gaussian or truncated (interrupted) control with the pulse area of 2π is sufficient to reach near-optimal operation. In a practical setting, such simplicity in combination with the lower Rabi frequency requirement of ATS memory would reduce technical complexity substantially by eliminating demand for wide-bandwidth electronics and optical components to shape the optimal control fields.

Robustness to decoherence. For spin-wave-based quantum memory protocols, memory efficiency for a given storage time strongly depends on the spin decoherence, which may have different sources, including magnetic field inhomogeneity, that lifts the degeneracy of spin states involved in the storage. In general, spin-wave decay (decoherence) occuring between the write and read-out stages degrades the memory efficiency irrespective of the protocol used: it is an exponential decay of the efficiency versus storage time. However, reduction in the efficiency due to decoherence during the writing and reading stages depends on the duration of the input signal field and how fast writing and read-out is carried out, which depends on the protocol. In the limit that $d \gg 1$ and $\gamma_s \ll \gamma_e$, where γ_s is spin-decoherence rate, for adiabatic memory protocols this effect can be minimized by choosing a short signal duration ($\tau \ll 1/\gamma_e$) that can still satisfy the adiabaticity condition, $d\tau\gamma_e \gg 1$. However, in the limited-optical-depth regime, this selection is quite restricted, making fast storage/retrieval schemes such as the ATS protocol more favourable over the adiabatic protocols such as EIT and Raman[40]. In particular, in the regime where γ_s is comparable to γ_e, and where optical depth is relatively small ($d < 10$) as in our experimental conditions, the difference between these approaches becomes much more distinct. Under these conditions, optimal EIT/Raman-based storage requires storage of long pulses $\tau > 1/\gamma_e$ such that $\tau d\gamma_e \gg 1$, whereas the ATS scheme can perform optimal storage with much shorter pulses (since it only requires $d\gamma_e \sim 1$), which suffer from decoherence much less and thus lead to much larger memory efficiency, as shown in Fig. 2e.

We note that Raman memory is expected to be more robust compared with EIT due to far-off-resonant operation, which relaxes the general adiabaticity condition, thereby allowing for relatively shorter pulse storage, as shown in our experiments. But at the same time, the large detuning ($\Delta \gg \gamma_e$) weakens the effective coupling, and together with limited control power, it leads to inefficient memory in the low-optical-depth regime.

Finally, we point out that the robustness of the ATS memory compared with EIT memory is rooted in the fundamental phenomenological difference between ATS (a.c. Stark splitting) and EIT (quantum interference), which are the native operating regimes of these protocols, respectively. Each regime ideally requires $\gamma_s \ll \gamma_e$, but to a completely different extent. For example, when the γ_s is comparable to γ_e, the EIT transmission dip cannot be observed due to the fragility of the quantum interference against decoherence. But under the same conditions, the ATS features can still be observed, though with additional broadening in the width of the ATS peaks, which is not an obstacle for a workable implementation. This shows that in the systems having large decoherence, photon storage and manipulation via the ATS scheme is much more feasible than the EIT scheme. Furthermore, in this article we have focused only on the implementation of the ATS protocol in a Λ-type three-level system involving spin-levels for the purpose of long-lived storage. There are some other systems that cannot allow EIT due to similar decoherence rates between the levels involved[60]. In contrast, our scheme can be easily implemented in these systems, thus making them potentially accessible for coherent storage and/or manipulation of photons.

Storage and retrieval fidelity. Memory fidelity, which measures the overlap between the input and retrieved quantum states, is one of the most important metrics for the suitability of quantum devices for applications in quantum information processing. Degradation from unity storage fidelity may arise from different effects, such as phase transformations, unbalanced spin degeneracy, pulse distortions and photonic noise. While most of these effects can be compensated or fixed with optimization, the noise added by a memory operation is the most

serious problem for such applications. An example of such photonic noise is the technical noise that requires spectral and/or spatial filtering of signal from the strong control field. As discussed earlier, the smaller control power requirement of the ATS scheme reduces complexity of the filtering techniques. Other kinds of photonic noise more fundamental in nature, such as four-wave mixing noise that cannot be eliminated by the standard filtering techniques, are significant obstacles for faithful spin-wave-based memories. Based on the lower power demand, we anticipate that this issue will not be a limiting factor for ATS memory, particularly when compared with broadband Raman memory[58], although it requires more detailed investigation. To back up this claim, in our experiments, we have demonstrated the single-photon level operation of ATS memory with no measurable four-wave mixing noise. While we achieve a large signal-to-noise ratio (SNR = 40) for storage of signal pulses with mean photon number as low as 0.3, we find that the residual noise component is mainly due to the scattered control field, which can be easily removed with a spectral filter. These results show that ATS memory holds great promise for high-fidelity storage and retrieval of quantum states encoded into short pulses.

Technical complexity. Technical complexity of a quantum memory protocol depends on two factors: (1) intrinsic operational principle and (2) limitations arising from the atomic platform that is most compatible with the protocol. Regarding the first factor, all-optical based memories such as EIT, ATS and Raman have significant advantages over some of photon-echo type memories such as CRIB[54,55], GEM[56] and Raman-GEM[21] protocols, which are based on controlled reversible broadening of the relevant absorption feature via magnetic- or electric-field gradients. In particular, the implementation of fast storage/retrieval with electric- or magnetic-field-controlled photon-echo memories is technically very challenging despite their inherent broadband capacity. In this respect, the ATS memory protocol combines favourable broadband scaling of the photon-echo techniques with the technical simplicity of all-optical based EIT/Raman type memories. With these desirable features, the ATS scheme resembles the AFC protocol, which mediates storage process through a comb-shaped absorption profile without need of any actively controlled broadening. In this situation, apart from the exceptional

temporal/spectral multiplexing storage capacity of the AFC scheme[42], the technical complexity of the ATS protocol with respect to the AFC scheme can be evaluated on the basis of the second factor, related to the limitations arising from atomic media. The implementation of an AFC in rare-earth ion doped solids, which are most suitable media due to their inhomogeneously broadened line that can be shaped into a comb, requires advanced persistent-hole-burning techniques with very stable laser systems. Furthermore, rare-earth systems that are suitable with spin-wave-based AFC protocol, such as Pr^{3+} and Eu^{3+} have very small hyperfine splittings[43] that limit the bandwidth of an AFC memory for practical use[22]. In contrast, the implementation of ATS memory, for example, in cold atoms featuring homogeneously broadened transition line, does not require such preparation, as the absorption peaks are dynamically generated via a.c. Stark splitting. Also, this feature provides versatile operation such as variable peak spacing and dynamic control of the memory bandwidth, which is not possible with spectral-hole burning based AFC memory. Finally, the bandwidth of ATS memory in alkali atomic gases, being most suitable medium with large hyperfine splitting, can approach the gigahertz regime, in contrast to the few-megahertz bandwidth possible in AFC memory using well-known spin-wave-compatible rare-earth systems.

Data availability
The data that support the plots within this paper and other findings of this study are available from the corresponding authors upon reasonable request.

References
58. Bustard, P. J., England, D. G., Heshami, K., Kupchak, C. & Sussman, B. J. Reducing noise in a Raman quantum memory. *Opt. Lett.* **41**, 5055–5058 (2016).
59. Nunn, J. et al. Theory of noise suppression in Λ-type quantum memories by means of a cavity. *Phys. Rev. A* **96**, 012338 (2017).
60. Khan, S., Bharti, V. & Natarajan, V. Role of dressed-state interference in electromagnetically induced transparency. *Phys. Lett. A* **380**, 4100–4104 (2016).